

Visualization of subcycle nonadiabatic-nondipole coupling in strong-field ionization

Xiaodan Mao ¹, Hongcheng Ni ^{1,2,*} and Jian Wu ^{1,2,3}

¹State Key Laboratory of Precision Spectroscopy, East China Normal University, Shanghai 200241, China

²Collaborative Innovation Center of Extreme Optics, Shanxi University, Taiyuan, Shanxi 030006, China

³Chongqing Key Laboratory of Precision Optics, Chongqing Institute of East China Normal University, Chongqing 401121, China



(Received 31 August 2024; revised 3 November 2024; accepted 2 December 2024; published 16 December 2024)

Light-matter interaction involves the transfer of both energy and linear momentum to matter. In the context of strong-field tunneling ionization, they are manifested as nonadiabatic and nondipole effects, respectively, which have been shown to interact on the subcycle scale. In this work we propose two experimentally feasible protocols for direct visualization of the subcycle interplay between nonadiabatic and nondipole tunneling effects. These protocols hinge on the intersection of the average linear momentum transferred to the released photoelectron at a specific photoemission angle, with the magnitude of this intersection serving as an indicator of the coupling strength. In addition, by defining the instantaneous effective angular frequency of the laser field, we have formulated analytical expressions that provide a quantitative description of the coupling effect. Our results provide a clear and intuitive approach to visualizing the impact of the subcycle nonadiabatic-nondipole coupling effects, thereby enhancing our comprehension of the time-resolved tunneling process through which light imparts both energy and linear momentum to electrons.

DOI: [10.1103/PhysRevA.110.063113](https://doi.org/10.1103/PhysRevA.110.063113)

I. INTRODUCTION

Light possesses both energy and linear momentum. In the process of strong-field ionization, these properties are imparted from light to matter. The energy from the light liberates the bound electron, ejecting it into the continuum and resulting in ionization. Once the ionization potential is surmounted, the residual absorbed energy is evident in the photoelectron momentum distribution (PMD), manifested as a nonzero radius perpendicular to the laser propagation direction. The transfer of energy is commonly addressed within the framework of dipole approximation, which is a typical practice in the study of strong-field ionization. However, this approximation results in a symmetric distribution of the PMD along the light propagation direction, which does not account for the transfer of linear momentum of light to matter. To fully capture linear momentum transfer, it is necessary to extend beyond the dipole approximation and incorporate nondipole effects of higher-order multipole interactions [1–4].

In the context of strong-field tunneling ionization, the transfer of light energy and linear momentum is manifested as nonadiabatic and nondipole effects, respectively, both of which have attracted significant interest and have become central subjects of ongoing research discussions. The periodic oscillation of the laser field, rather than being static, leads to the transfer of light energy to the ionized electron during the tunneling process, known as nonadiabatic effects [5–7]. The degree of nonadiabaticity during tunneling can be characterized by the Keldysh parameter $\gamma = \frac{\omega}{F} \sqrt{2I_p}$, where ω is the laser angular frequency, F is the laser electric field amplitude,

and I_p is the ionization potential of the atom or molecule being ionized. When $\gamma \rightarrow 0$, tunneling ionization can be deemed adiabatic; when $\gamma \sim 1$, it indicates ionization in the nonadiabatic tunneling regime. Nonadiabatic effects during the tunneling process plays an important role in strong-field ionization [7–12]. In adiabatic tunneling, the initial transverse momentum of the ionized electron is centered at zero [13,14]. Conversely, in nonadiabatic tunneling, the bound electron tunnels with a transverse momentum that is centered around a nonzero value, and the tunneling occurs closer to the nucleus compared to the adiabatic case [7]. In the presence of an elliptically polarized laser field, nonadiabatic corrections to the initial transverse momentum of the electron can significantly influence the photoelectron angular distribution [15–17]. With circularly polarized laser, nonadiabatic effects facilitate selective depletion of electrons from p orbitals that are counterrotating with respect to the laser [18,19]. In 2018 direct evidence for nonadiabatic effects was provided experimentally, and the effective angular frequency has been introduced to quantify their impact [20]. In essence, nonadiabatic effects intertwine with various strong-field ionization phenomena by altering the position, momentum, and energy of the electron at the tunnel exit.

The dispersion relation of a photon, given by $p = E/c$, where p is the photon momentum, E is its energy, and c is the light speed in vacuum, indicates that the photon linear momentum is very small, making its effects less noticeable compared to energy absorption. However, advances in detection technology have recently enabled the clear identification of even these minute linear momentum transfers induced by nondipole effects. In 2011 the linear momentum transfer along the laser propagation direction was first experimentally observed during the ionization of argon and neon atoms with

*Contact author: hcnl@lps.ecnu.edu.cn

circularly polarized laser fields [21]. Following this, a transfer of linear momentum in the opposite direction was identified in strong-field ionization using linearly polarized laser fields, which was attributed to the interplay between the magnetic field and the Coulomb potential [22]. Additionally, the sub-cycle transfer of linear momentum in strong-field tunneling ionization was investigated experimentally [23]. The precision of the measurement has since been significantly enhanced through the use of two counterpropagating laser pulses, which clearly determined the zero point in the linear momentum distribution [24]. Concurrently, a number of theoretical studies have been carried out to dissect this linear momentum transfer. The linear momentum transfer during the under-barrier motion in tunneling ionization has been studied [25]. It has been further analyzed under both single-photon and tunneling ionization [26]. These findings have gained experimental support [24,27,28]. Remarkably, linear momentum transfer in double ionization has also been investigated in both the single-photon [29] and tunneling limits [30]. In addition, the relationship between linear momentum transfer and the minimum number of photons required to reach the ionization threshold has been investigated [31]. Moreover, individual contributions of electric quadrupole and magnetic dipole interactions have been successfully separated [32–34]. Furthermore, in the case of above-threshold ionization, the energy conservation is influenced by nondipole effects, which are evident as a common offset of U_p/c to the ATI rings against the laser propagation direction [35–37], where U_p is the ponderomotive potential.

The energy and momentum of a photon are intrinsically linked, which naturally leads to the coupling of nonadiabatic and nondipole effects during the process of strong-field tunneling ionization. Recently, a theoretical framework for subcycle linear momentum transfer has been developed [38], illustrating that these effects interact on the subcycle timescale. In this study we propose two experimentally feasible protocols designed to directly visualize the subcycle nonadiabatic-nondipole coupling in strong-field tunneling ionization.

The paper is organized as follows: Sec. II provides a brief overview of the theoretical approaches. Section III describes the schemes for shaping the laser fields to visualize the coupling effects. Section IV validates the proposed tailored laser fields by demonstrating the minimum distance of the electron to the ionic core during its continuum motion. Section V presents the characterization of coupling effects in linear momentum transfer, along with the derivation of their analytical expressions. Conclusions are given in Sec. VI. Atomic units (a.u.) are used unless stated otherwise.

II. THEORETICAL FRAMEWORK

In this section we provide a brief overview of the background of the nonadiabatic-nondipole coupling effects as well as the numerical methods and analytical approaches employed in our study. These include (a) the solution of the three-dimensional time-dependent Schrödinger equation (TDSE), which serves as a fundamental tool for describing the quantum dynamics of the system; (b) the nondipole saddle-point approximation (ndSPA), an advanced method that incorporates both nondipole and nonadiabatic effects, allowing it to

capture the nonadiabatic-nondipole coupling phenomena in an analytical manner; (c) the nondipole Ammosov-Delone-Krainov (ndADK) theory, which is applicable in the adiabatic limit and does not account for nonadiabatic-nondipole coupling. By comparing the outcomes of these different methods, we can effectively distinguish the influence of coupling effects. The TDSE solution is utilized to confirm the accuracy and relevance of the approximations made within the ndSPA framework.

A. Nonadiabatic-nondipole coupling

Tunneling ionization can be conceptualized as a two-stage process, encompassing quantum tunneling through the potential barrier and the subsequent classical motion of the released electron in the continuum. Accordingly, the asymptotic linear momentum transfer along the laser propagation direction (\hat{e}_z) can be apportioned into two distinct contributions [38]:

$$\langle p_z \rangle = \langle v_z \rangle + \frac{\Delta E}{c} \quad (1)$$

for direct ionization where electron rescattering is absent, where $\langle p_z \rangle$ and $\langle v_z \rangle$ represent the average linear momentum transfer in the asymptotic region and at the tunnel exit, respectively, and ΔE denotes the energy absorption of the electron in the continuum motion. In our present study, electron rescattering is avoided in our specifically tailored laser fields. Since there is no laser field component in the propagation direction, the Coulomb-laser coupling is absent, making the effect of the Coulomb interaction on the linear momentum transfer negligible [38]. Therefore, the influence of Coulomb potential is not considered in the following analytical derivation of the linear momentum transfer. In Eq. (1) the first term

$$\langle v_z \rangle = \frac{2I_p + \langle v_\perp^2 \rangle}{6c} (1 - \delta), \quad (2)$$

reflecting the linear momentum accumulated during the quantum tunneling stage, where the subscript \perp denotes quantities within the polarization plane, v_\perp stands for the initial transverse momentum at the tunnel exit, and $\delta = (2\alpha_Z F)/(2I_p)^{3/2}$ with $\alpha_Z = 1 + Z/\sqrt{2I_p}$ and $Z = 1$ the asymptotic charge of the residual ion. The second term $\Delta E/c$ accounts for the linear momentum transfer accumulated during the motion of the released electron in the continuum and is expressed as

$$\frac{\Delta E}{c} = \frac{\langle p_\perp^2 \rangle - \langle v_\perp^2 \rangle}{2c}, \quad (3)$$

where p_\perp is the component of the asymptotic momentum within the polarization plane. Given the relation $\mathbf{p}_\perp = \mathbf{v}_\perp - \mathbf{A}$, where \mathbf{A} denotes the vector potential of the laser field. Equation (3) can then be rewritten as

$$\frac{\Delta E}{c} = \frac{\langle A^2 \rangle}{2c} - \frac{\langle \mathbf{v}_\perp \rangle \cdot \mathbf{A}}{c}. \quad (4)$$

Note further

$$\langle v_\perp^2 \rangle = \langle v_\perp \rangle^2 + \frac{F}{2\sqrt{2I_p}}, \quad (5)$$

the final linear momentum transfer, as given in Eq. (1), can then be reorganized into

$$\begin{aligned} \langle p_z \rangle &= \langle p_z \rangle^{(A)} + \langle p_z \rangle^{(NA)} \\ &= (1 - \delta) \underbrace{\left(\frac{I_p}{3c} + \frac{F}{12c\sqrt{2I_p}} \right)}_A + \frac{\langle A^2 \rangle}{2c} \\ &\quad + (1 - \delta) \underbrace{\left(\frac{\langle v_\perp \rangle^2}{6c} - \frac{\langle \mathbf{v}_\perp \rangle \cdot \mathbf{A}}{c} \right)}_{NA}, \end{aligned} \quad (6)$$

which comprises two contributions, i.e., from pure adiabatic tunneling $\langle p_z \rangle^{(A)}$ and from coupling to nonadiabatic effects $\langle p_z \rangle^{(NA)}$. When nonadiabaticity is absent, we have $\langle v_\perp \rangle = 0$, and $\langle p_z \rangle^{(NA)}$ vanishes. Therefore, the nonadiabatic term, $\langle p_z \rangle^{(NA)}$, arises from nonadiabatic-nondipole coupling. Although the initial transverse momentum induced by nonadiabaticity, $\langle v_\perp \rangle$, is typically not large, its impact is amplified when coupled with the vector potential, as evident in the last term of Eq. (6), $-\langle \mathbf{v}_\perp \rangle \cdot \mathbf{A}/c$. This behavior makes the nonadiabatic-nondipole coupling experimentally discernible in the asymptotic PMD. However, a direct observation of such coupling has remained elusive.

In this study we propose two experimentally feasible protocols designed to directly visualize the subcycle nonadiabatic-nondipole coupling in strong-field tunneling ionization. We also provide analytical expressions to quantify the strength of the coupling effect. Our approach hinges on the separate manipulation of $\langle p_z \rangle^{(A)}$ and $\langle p_z \rangle^{(NA)}$. This is possible by independently varying the degree of nonadiabaticity while keeping the vector potential fixed. The degree of nonadiabaticity can be controlled by tailoring the instantaneous effective angular frequency of the laser field [11,20]. Importantly, there is a direct relationship between the coupling strength and the degree of nonadiabaticity. Consequently, the linear momentum transfer $\langle p_z \rangle$ is governed by the coupling strength.

B. Time-dependent Schrödinger equation

We solve the three-dimensional TDSE to numerically simulate strong-field ionization of the helium atom. Earlier studies [39] have shown that electron correlation is negligible for the helium atom in the attoclock setting, and thus we stick with the single-active-electron approximation. The nondipole Hamiltonian is given by [24,34,38,40]

$$\begin{aligned} H &= \frac{1}{2} \left[\mathbf{p} + \mathbf{A}(t) + \frac{\hat{\mathbf{e}}_z}{c} \left(\mathbf{p} \cdot \mathbf{A}(t) + \frac{A^2(t)}{2} \right) \right]^2 \\ &\quad + V\left(\mathbf{r} - \frac{z}{c}\mathbf{A}(t)\right) \end{aligned} \quad (7)$$

with the Coulomb potential

$$V(r) = -\frac{1 + e^{-r^2/2}}{\sqrt{r^2 + a_0}}. \quad (8)$$

The soft-core parameter $a_0 = 0.14328$ is adjusted to match the experimental ground-state energy $E_0 = -I_p = -0.90357$ a.u. of helium.

The TDSE is solved numerically on a spatial grid with 1024 points in each dimension, using a spatial step of $\Delta x = 0.2$ a.u. and a time step of $\Delta t = 0.02$ a.u. The time evolution is carried out using the split-operator Fourier method, which is applicable since the space operator and the momentum operator in the nondipole Hamiltonian [Eq. (7)] are separated. To prevent reflections of the wave function at the grid border, we implement an absorbing boundary, taking the form $1/[1 + \exp\{(r - r_0)/d\}]$, where $r_0 = 87.4$ and $d = 4$ a.u. As the electron wave packet approaches r_0 , it is attenuated by the mask function. In the calculations, we perform absorption on the wave function every 0.2 a.u. in time, and we have tested that the results are converged with respect to this time span as well as other grid parameters. The final PMD $W_{\text{TDSE}}(\mathbf{p})$ is obtained by cumulatively projecting the absorbed wave function onto the nondipole Volkov state [31,41]

$$\psi_p(t) = \exp \left[i\mathbf{p} \cdot \mathbf{r} - i \int^t \frac{1}{2} \boldsymbol{\pi}^2(\tau) d\tau \right], \quad (9)$$

where $\boldsymbol{\pi}(t) = \mathbf{p} + \mathbf{A}(t) + (\hat{\mathbf{e}}_z/c)[\mathbf{p} \cdot \mathbf{A}(t) + A^2(t)/2]$. The average linear momentum transfer at the end of laser field is given by

$$\langle p_z \rangle = \frac{\int W(\mathbf{p}) p_z d\mathbf{p}}{\int W(\mathbf{p}) d\mathbf{p}}, \quad (10)$$

where the ionization rate $W(\mathbf{p}) = W_{\text{TDSE}}(\mathbf{p})$.

C. Nondipole saddle-point approximation

We delve into an analytical investigation of the subcycle nonadiabatic-nondipole coupling using the framework of nondipole strong-field approximation (ndSFA). Here we disregard the minor influence of the Coulomb potential on the linear momentum transfer. Through the application of nondipole saddle-point approximation (ndSPA), the tunneling ionization rate is given by [42–44]

$$W_{\text{ndSPA}}(\mathbf{p}) = |\dot{S}|^{-\alpha z} \exp[-2\text{Im}S], \quad (11)$$

where the nondipole action is given by the expression $S = -\int_{t_s}^{t_r} \{[\mathbf{p} + \mathbf{A}(t) + (\hat{\mathbf{e}}_z/c)[\mathbf{p} \cdot \mathbf{A}(t) + A^2(t)/2]]^2/2 + I_p\} dt$. The complex saddle-point time $t_s = t_r + it_i$ is obtained by solving the saddle-point equation

$$\frac{1}{2} \left[\mathbf{p} + \mathbf{A}(t_s) + \frac{\hat{\mathbf{e}}_z}{c} \left(\mathbf{p} \cdot \mathbf{A}(t_s) + \frac{1}{2} A^2(t_s) \right) \right]^2 + I_p = 0, \quad (12)$$

where $t_r = \text{Re} t_s$ represents the ionization time and $t_i = \text{Im} t_s$ is related to the tunneling ionization rate.

Rearranging the imaginary part of the saddle-point equation [Eq. (12)] gives

$$i \left(1 + \frac{p_z}{c} \right) [\mathbf{k}_\perp \cdot \text{Im}\mathbf{A}(t_s)] = 0, \quad (13)$$

where $\mathbf{k}_\perp = \mathbf{p}_\perp + \text{Re}\mathbf{A}(t_s)$. Therefore, by choosing the auxiliary momentum k_\perp as [7,38]

$$\mathbf{k}_\perp = [\mathbf{p} + \text{Re}\mathbf{A}(t_s)] \cdot \frac{-\text{Im}A_y(t_s)\hat{\mathbf{e}}_x + \text{Im}A_x(t_s)\hat{\mathbf{e}}_y}{\sqrt{[\text{Im}A_x(t_s)]^2 + [\text{Im}A_y(t_s)]^2}}, \quad (14)$$

the imaginary part of the saddle-point equation [Eq. (13)] is fulfilled automatically. Thereby, the search for the

saddle-point time in the full complex plane is reduced to a one-dimensional root-finding problem for the real part of the saddle-point equation. This approach, using the (t_r, k_\perp, p_z) coordinate system, greatly enhances computational efficiency in the ndSPA calculations. It is important to account for the Jacobian of the coordinate transformation when calculating the ionization rate:

$$\tilde{W}_{\text{ndSPA}}(t_r, k_\perp, p_z) = \left| \det \frac{\partial(p_x, p_y, p_z)}{\partial(t_r, k_\perp, p_z)} \right| W_{\text{ndSPA}}(\mathbf{p}), \quad (15)$$

which is then substituted into Eq. (10) to calculate the average linear momentum transfer.

D. Nondipole Ammosov-Delone-Krainov theory

The ndSPA approach fully includes nonadiabatic tunneling effects, making it a suitable tool for analyzing nonadiabatic-nondipole coupling. To provide a comparative analysis, an approach that excludes nonadiabaticity is essential. We derive the adiabatic limit of ndSPA, termed as ndADK, to serve this purpose. We first expand the vector potential $\mathbf{A}(t_s)$ up to the first order in the small imaginary time t_i (corresponding to a small Keldysh parameter $\gamma \approx \omega t_i$),

$$\mathbf{A}(t_s = t_r + it_i) \approx \mathbf{A}(t_r) - it_i \mathbf{F}(t_r). \quad (16)$$

This expansion omits higher-order terms related to the electric field derivatives, under the assumption that the intense laser field can be considered quasistatic during adiabatic tunneling. Substituting this approximation into the saddle-point equation [Eq. (12)] and retaining terms up to t_i yields the imaginary part of the equation

$$-it_i \left(1 + \frac{p_z}{c}\right) [\mathbf{k}_\perp \cdot \mathbf{F}(t_r)] = 0, \quad (17)$$

where the auxiliary momentum $\mathbf{k}_\perp = \mathbf{p}_\perp + \mathbf{A}(t_r)$ is equivalent to the transverse momentum at the tunnel exit \mathbf{v}_\perp , differing from the definition used in ndSPA. Its value is given by

$$\mathbf{k}_\perp = [\mathbf{p} + \mathbf{A}(t_r)] \cdot \frac{F_y(t_r)\hat{\mathbf{e}}_x - F_x(t_r)\hat{\mathbf{e}}_y}{F(t_r)}, \quad (18)$$

which ensures that the imaginary part of the saddle-point equation [Eq. (17)] is always satisfied. Organizing the real part of the saddle-point equation results in

$$t_i = \sqrt{\frac{2I_p + k_\perp^2 + p_z^2 - \frac{p_z}{c}(p_\perp^2 - k_\perp^2)}{\left(1 + \frac{p_z}{c}\right)F^2(t_r)}}. \quad (19)$$

Substituting Eq. (19) into Eq. (11) for the ionization rate, we obtain

$$\begin{aligned} \text{Im } S &= I_p t_i + \frac{1}{2} \text{Re} \int_0^{t_i} \\ &\times \left\{ \mathbf{p} + \mathbf{A}(t_s) + \frac{\hat{\mathbf{e}}_z}{c} \left[\mathbf{p} \cdot \mathbf{A}(t_s) + \frac{1}{2} A^2(t_s) \right] \right\}^2 dt \\ &= \frac{[2I_p + k_\perp^2 + p_z^2 - \frac{p_z}{c}(p_\perp^2 - k_\perp^2)]^{3/2}}{3F\sqrt{1 + \frac{p_z}{c}}} \end{aligned} \quad (20)$$

and

$$\begin{aligned} |\ddot{S}|^{-\alpha z} &= \left| i \left(1 + \frac{p_z}{c}\right) t_i F^2(t_r) \right|^{-\alpha z} \\ &= \left[\left(1 + \frac{p_z}{c}\right) \left(2I_p + k_\perp^2 + p_z^2 - \frac{p_z}{c}(p_\perp^2 - k_\perp^2)\right) F^2 \right]^{-\alpha z/2}. \end{aligned} \quad (21)$$

The ndADK ionization rate is thus given by

$$\begin{aligned} W_{\text{ndADK}}(\mathbf{p}) &\approx \left[\left(1 + \frac{p_z}{c}\right) \left(2I_p + k_\perp^2 + p_z^2 - \frac{p_z}{c}(p_\perp^2 - k_\perp^2)\right) F^2 \right]^{-\alpha z/2} \\ &\times \exp \left\{ -\frac{2[2I_p + k_\perp^2 + p_z^2 - \frac{p_z}{c}(p_\perp^2 - k_\perp^2)]^{3/2}}{3F\sqrt{1 + \frac{p_z}{c}}} \right\}, \end{aligned} \quad (22)$$

which reduces to the typical dipole ADK theory for $c \rightarrow \infty$. Since the calculations are performed within the (t_r, k_\perp, p_z) coordinate system, the Jacobian of the transformation must be considered:

$$\left| \det \frac{\partial(p_x, p_y, p_z)}{\partial(t_r, k_\perp, p_z)} \right| \approx \left| \frac{k_\perp [F_x(t_r)\dot{F}_y(t_r) - \dot{F}_x(t_r)F_y(t_r)]}{F^2(t_r)} + F(t_r) \right|. \quad (23)$$

Likewise, we can obtain the average linear momentum transfer by substituting the ionization rate [Eq. (22)] together with the Jacobian factor [Eq. (23)] into Eq. (10).

III. CHOICE OF LASER FIELD

In this section we present two distinct categories of laser fields, crafted for the explicit purpose of directly visualizing the subcycle nonadiabatic-nondipole coupling effects. These laser fields are selected for their two essential features:

(1) The instantaneous vector potential is deliberately maintained at a specific value. This strategy ensures that the contribution to the linear momentum transfer from adiabatic tunneling processes remains consistent, providing a stable baseline for observation.

(2) The degree of coupling effects is independently adjustable. This is achieved by precisely controlling the effective angular frequency of the laser field using a tailored laser field. This tunability allows for the systematic exploration of how nonadiabatic-nondipole coupling influences the linear momentum transfer.

By fulfilling these conditions, we ensure that any observed variations in the linear momentum transfer are attributable solely to nonadiabatic-nondipole coupling, thereby enabling a clear and unambiguous analysis of these effects in strong-field ionization.

A. Elliptically polarized laser field

In order to visualize the coupling effects, we need to independently adjust the nonadiabaticity through the instantaneous effective angular frequency while keeping the amplitude of the instantaneous vector potential fixed at a certain angle. In this sense, elliptically polarized (EP) laser fields

serve as great candidates, where we keep the field strength along the x direction fixed while varying the intensity along the y direction. Thus, we introduce the first category of laser fields utilized in our study to implement the idea: EP fields with varying ellipticity. Specifically, we have selected a set of laser fields with ellipticities $\varepsilon = 0.86, 1.0, 1.4$, as depicted in Fig. 1. The vector potential for these fields is defined by

$$\mathbf{A}_{\text{EP}}(t) = A_0 \cos(\omega t) \hat{\mathbf{e}}_x + \varepsilon A_0 \sin(\omega t) \hat{\mathbf{e}}_y, \quad (24)$$

and the corresponding electric field is given by

$$\mathbf{F}_{\text{EP}}(t) = F_0 \sin(\omega t) \hat{\mathbf{e}}_x - \varepsilon F_0 \cos(\omega t) \hat{\mathbf{e}}_y. \quad (25)$$

These laser fields are characterized by an angular frequency of $\omega = 0.057$ a.u. (corresponding to a wavelength of $\lambda = 800$ nm) and an electric field amplitude of $F_0 = 0.079$ a.u. For each ellipticity ε , the amplitude of the negative vector potential maintains a fixed value in the $\hat{\mathbf{e}}_x$ direction while it varies in the $\hat{\mathbf{e}}_y$ direction. The temporal envelope of the vector potential of the laser pulse is shaped by the function $\cos^4(\omega t/2N)$ over a total of $N = 15$ cycles. In the case of the long pulse under consideration, the influence of the envelope on the overall dynamics is negligible, and therefore, we have not explicitly included it in the mathematical expressions for the vector potential and electric field of the laser. Our analysis has confirmed that whether the coupling features can be observed is independent of the specific pulse duration.

The EP fields can be obtained experimentally with the setup as in Ref. [11]. An amplified Ti:sapphire femtosecond laser system can be used to generate the laser pulses. Their ellipticity is controlled by inserting a wire grid polarizer before a $\lambda/4$ wave plate, which is fixed with its fast axis along the x direction. Before each experimental data acquisition, the total input pulse intensity is adjusted, and a second wire grid polarizer is used to ensure that the x component of the pulse intensity remains constant at different ellipticities.

At the specific time $t = \pi/\omega$ as indicated by black dashed lines in Fig. 1, the vector potential stays as $\mathbf{A} = -A_0 \hat{\mathbf{e}}_x$ across all three laser fields, while their respective electric fields differ. Considering that the adiabatic term $\langle p_z \rangle^{(A)}$ in the linear momentum transfer [Eq. (6)] is primarily associated with the vector potential and minimally affected by the electric field, the values of this adiabatic term remain nearly identical across the different ellipticities of the laser fields studied. This consistency in the adiabatic term allows us to isolate and examine the variations in nonadiabatic-nondipole coupling effects as a function of ellipticity.

We now turn to the nonadiabatic-nondipole coupling term $\langle p_z \rangle^{(\text{NA})}$ in Eq. (6). When the electron gets ionized at $t = \pi/\omega$, the electric field is given by $\mathbf{F} = \varepsilon F_0 \hat{\mathbf{e}}_y$, the corresponding vector potential is $\mathbf{A} = -A_0 \hat{\mathbf{e}}_x$, and the electron eventually emits along the $\hat{\mathbf{e}}_x$ direction. At this specific time, the initial transverse momentum \mathbf{v}_\perp at the tunnel exit and the instantaneous vector potential \mathbf{A} are antiparallel. We introduce the instantaneous effective angular frequency ω_{eff} [20,45,46]

$$\omega_{\text{eff}} = \frac{\partial}{\partial t} \arctan\left(\frac{F_y}{F_x}\right) \quad (26)$$

evaluated at the angle $\phi = \arctan(-A_y/-A_x)$, which, in the absence of the Coulomb potential, is approximately equal to

the photoemission angle $\phi_p = \arctan(p_y/p_x)$. The instantaneous effective angular frequency ω_{eff} serves to quantitatively describe the nonadiabatic effects, as shown in Fig. 1(c). A higher ω_{eff} signifies a greater instantaneous frequency of the electric field, corresponding to more pronounced nonadiabatic effects, and in turn more pronounced nonadiabatic-nondipole coupling.

Interestingly, by redefining the initial transverse momentum, k_\perp or v_\perp , in terms of the effective angular frequency ω_{eff} , we can derive a closed form of the nonadiabatic-nondipole coupling term $\langle p_z \rangle^{(\text{NA})}$, which is governed by ω_{eff} , as we will show later. This allows us to establish a direct link between the linear momentum transfer and the coupling effects through the effective angular frequency ω_{eff} .

B. Corotating and counterrotating two-color circularly polarized laser field

Besides the EP fields, any laser field that meets features 1 and 2 listed at the beginning of Sec. III can fulfill our requirements. The corotating (CoRTC) and counterrotating two-color (CRTC) circularly polarized laser fields naturally satisfy feature 1, where the vector potential amplitudes in the $\hat{\mathbf{e}}_x$ direction can be kept equal. Additionally, the instantaneous effective angular frequency is influenced by the amplitude ratio of the frequency-doubled laser field with respect to the fundamental one. Hence, we introduce the second category of laser fields consisting of CoRTC and CRTC fields, defined by the vector potential

$$\begin{aligned} \mathbf{A}_{\text{TC}}(t) = & A_0 \left[\cos(\omega t) + \frac{\eta}{2} \cos(2\omega t) \right] \hat{\mathbf{e}}_x \\ & + A_0 \left[\sin(\omega t) + \varepsilon \frac{\eta}{2} \sin(2\omega t) \right] \hat{\mathbf{e}}_y, \end{aligned} \quad (27)$$

and the corresponding electric field

$$\begin{aligned} \mathbf{F}_{\text{TC}}(t) = & F_0 [\sin(\omega t) + \eta \sin(2\omega t)] \hat{\mathbf{e}}_x \\ & - F_0 [\cos(\omega t) + \varepsilon \eta \cos(2\omega t)] \hat{\mathbf{e}}_y, \end{aligned} \quad (28)$$

with a fundamental angular frequency $\omega = 0.057$ a.u. (corresponding to a wavelength of $\lambda = 800$ nm), an electric field amplitude $F_0 = 0.084$, a field amplitude ratio $\eta = 0.1$, and an ellipticity $\varepsilon = \pm 1$ ($\varepsilon = 1$ for the CoRTC field and $\varepsilon = -1$ for the CRTC field). The laser fields here have the same duration as the first category of EP laser fields.

The CoRTC and CRTC fields have been employed in various experiments [20,47–50]. A 250 μm β -barium borate crystal can be used to frequency double a 800 nm laser pulse to obtain the two-color laser fields. The fundamental and the second harmonic are separated by a dielectric beam splitter. The two laser pulses are configured with either the same or opposite helicity, then recombined and focused to form a CoRTC or CRTC field.

At the specific time $t = 0$ as indicated by black dashed lines in Fig. 2, the vector potentials for the CoRTC and CRTC fields are both $\mathbf{A} = A_0 \hat{\mathbf{e}}_x$, suggesting that the adiabatic contribution in their respective linear momentum transfers is the same. Additionally, the initial transverse momentum \mathbf{v}_\perp at the tunnel exit and the vector potential \mathbf{A} are antiparallel at this specific time $t = 0$. Similar to the previous EP fields, the mapping between $\langle p_z \rangle$ and the coupling effects can be

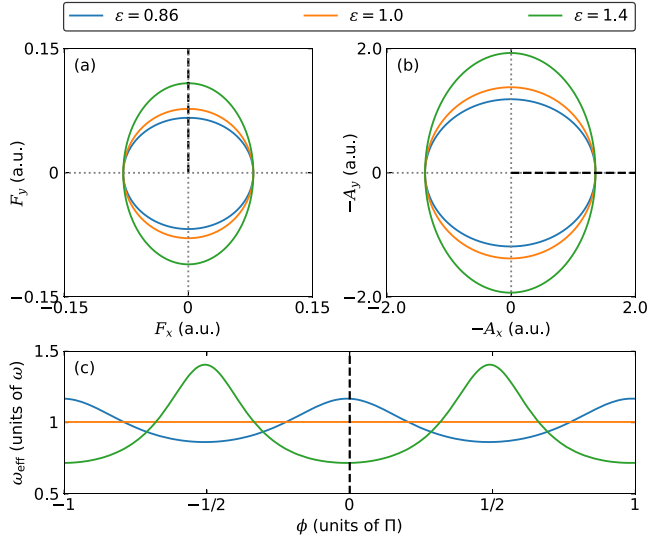


FIG. 1. Sketch of the elliptically polarized (EP) laser fields, including (a) the electric field $\mathbf{F}(t)$, (b) the negative vector potential $-\mathbf{A}(t)$, and (c) the effective angular frequency ω_{eff} as a function of ϕ for ellipticities $\varepsilon = 0.86$ (blue curves), $\varepsilon = 1.0$ (orange curves), and $\varepsilon = 1.4$ (green curves). The black dashed curves in all panels correspond to the same time $t = \pi/\omega$ and angle $\phi = 0$.

mediated by the effective angular frequency ω_{eff} , as shown in Fig. 2(c).

IV. CONTINUUM MOTION OF RELEASED ELECTRONS

In order to clearly visualize nonadiabatic-nondipole coupling, it is important to craft the laser fields where rescattering is avoided. To this end, we employ the classical-trajectory Monte Carlo (CTMC) method, with initial conditions derived from ndADK, to compute the ionization rates of electrons emitted at various times with different initial velocities. Additionally, we track their minimum distances from the atomic core during the continuum motion. The motion of the released electron in the presence of the laser field is governed by the Newtonian equations of motion. This calculation aims to validate the approach of considering only the direct ionization process in adiabatic tunneling scenarios. The validity of this approach in nonadiabatic tunneling is further supported by the consistency between ndSPA and TDSE calculations presented in Sec. V.

Figure 3 presents the ionization rate for electrons driven by EP fields in column (1), and their minimum distance r_{min} from the core during the continuum motion in column (2) for $\varepsilon = 0.86$ [row (a)] and $\varepsilon = 1.4$ [row (b)]. The data presented in column (2) represent $\log_{10}(r_{\text{min}})$. The blue-white region, indicating $r_{\text{min}} \approx 0$, signifies that electrons with initial conditions in this area are likely to return to the core during their motion. Conversely, the yellow-green regions correspond to $r_{\text{min}} \approx I_p/F$, suggesting that these electrons, once driven away by the laser fields, do not return to the core. The black lines represent the strength of the instantaneous electric field. Here $v_{\perp} < 0$ and $v_{\perp} > 0$ denote that the initial transverse momentum is aligned parallel or antiparallel to the instantaneous vector potential, respectively. The observations from

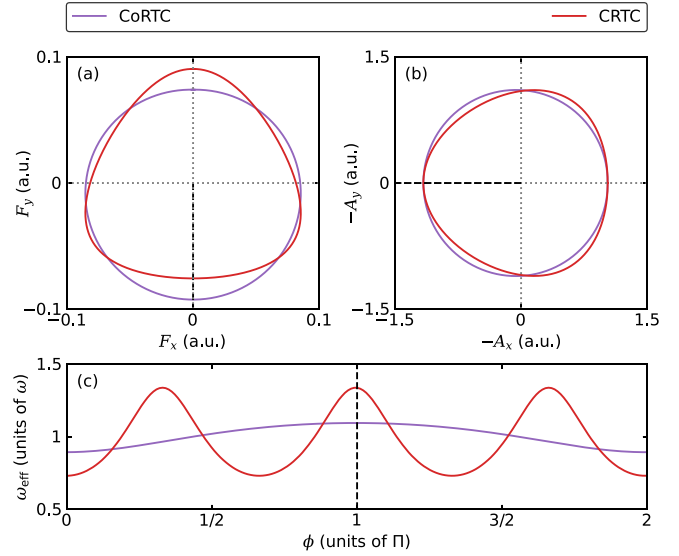


FIG. 2. Sketch of the corotating (CoRTC, purple curves) and counterrotating two-color (CRTC, red curves) circularly polarized laser fields, including (a) the electric field $\mathbf{F}(t)$, (b) the negative vector potential $-\mathbf{A}(t)$, and (c) the effective angular frequency ω_{eff} as a function of ϕ . The black dashed curves in all panels correspond to the same time $t = 0$ and angle $\phi = \pi$.

Fig. 3 indicate that in regions of high ionization probability, electrons do not return to the core, justifying the focus on direct ionization in our study due to the low likelihood of rescattering.

Similarly, Fig. 4 displays the ionization rates for electrons in CoRTC [row (a)] and CRTC [row (b)] fields in column (1), and their minimum distance r_{min} from the core in column (2). These results further demonstrate that the likelihood of an ionized electron returning to the core under the influence of these laser fields is very low.

Thus, the findings from both figures confirm that it is reasonable to concentrate on the direct ionization process for all laser field configurations studied, as the probability of rescattering events is minimal. This conclusion supports the use of Eq. (6) for calculating linear momentum transfer in EP, CoRTC, and CRTC fields.

V. VISUALIZATION OF SUBCYCLE NONADIABATIC-NONDIPOLE COUPLING

In this section we examine the characteristics of coupling effects by comparing the linear momentum transfer as a function of the photoemission angle across two categories of laser fields, highlighting the appearance of an intersection for the average linear momentum transfer at a specific angle. Additionally, we introduce the effective angular frequency of the laser field as a metric to gauge the strength of nonadiabatic-nondipole coupling on linear momentum transfer.

Employing TDSE, ndSPA, and ndADK, we illustrate the average linear momentum transfer $\langle p_z \rangle$ as a function of the photoemission angle $\phi_p = \arctan(p_y/p_x)$ in EP fields in Fig. 5. Results present in Fig. 5(a) are obtained using TDSE and ndSPA that fully include nonadiabatic tunneling

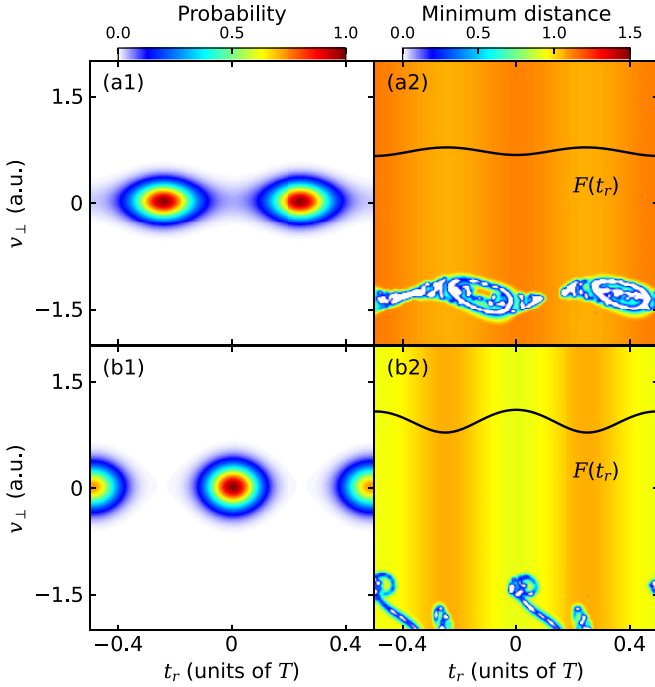


FIG. 3. The ionization rate [column (1)] and the minimum distance between the ionized electron and core [column (2)] calculated by the classical-trajectory Monte Carlo (CTMC) method with the initial conditions prepared by ndADK in the EP laser field with ellipticities $\varepsilon = 0.86$ [row (a)] and $\varepsilon = 1.4$ [row (b)]. In column (2), the black curves denote the magnitude of instantaneous electric field and the data are presented in the logarithmic scale.

effects and thus include nonadiabatic-nondipole coupling, while those shown in Fig. 5(b) are obtained using ndADK that neglect nonadiabatic effects and thus coupling effects are absent. From the figure, we have two observations. First, for all ellipticities studied, $\varepsilon = 0.86, 1.0, 1.4$, values of $\langle p_z \rangle$ in Fig. 5(a) surpass those in Fig. 5(b), indicating a positive contribution of coupling effects on $\langle p_z \rangle$. Second, a pronounced intersection in the average linear momentum occurs around $\phi_p = 0$ in Fig. 5(a) when nonadiabatic-nondipole coupling is included, as indicated by the shaded area, but this intersection is absent in Fig. 5(b). Given that the variation in $\langle p_z \rangle$ is on the order of 10^{-3} , which aligns with the resolution capable in experimental setups [24], the intersection is indeed detectable. This level of precision provides a feasible basis for observing the coupling effects under investigation, confirming the practical relevance of the intersection as a diagnostic tool in experimental contexts.

Our prior analysis confirms that the adiabatic contribution $\langle p_z \rangle^{(A)}(\phi_p = 0)$ is nearly identical across the three EP fields. In the adiabatic tunneling scenario, the coupling term $\langle p_z \rangle^{(NA)}(\phi_p = 0)$ vanishes, resulting in the absence of the intersection. However, in nonadiabatic tunneling, the coupling term $\langle p_z \rangle^{(NA)}(\phi_p = 0)$ varies in strength across the three EP fields, leading to the formation of the intersection at $\phi_p = 0$. Not surprisingly, the appearance of the intersection and the observation of nonadiabatic-nondipole coupling can be traced back to the initial conditions of the tunneled electrons. Shown

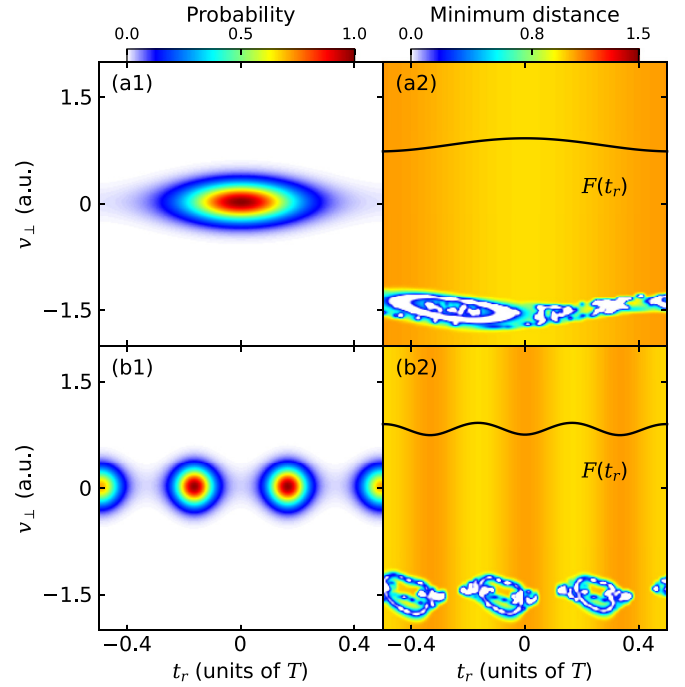


FIG. 4. The ionization rate [column (1)] and the minimum distance between the ionized electron and core [column (2)] calculated by the classical-trajectory Monte Carlo (CTMC) method with the initial conditions prepared by ndADK in the CoRTC field [row (a)] and the CRTC field [row (b)]. In column (2), the black curves denote the magnitude of instantaneous electric field and the data are presented in the logarithmic scale.

in Fig. 7 are the initial conditions prepared by the ndADK [row (a)] and ndSPA [row (b)] methods in the EP laser field with ellipticities $\varepsilon = 0.86$ [column (1)] and $\varepsilon = 1.4$ [column (2)]. The blue solid curves represent the average initial transverse momentum $\langle v_\perp \rangle$ as a function of ionization time t_r . Clearly, under adiabatic tunneling, $\langle v_\perp \rangle$ vanishes at all times, while for nonadiabatic tunneling, $\langle v_\perp \rangle$ has a finite value which modulates with time.

Remarkably, the appearance of Figs. 5(a) and 7(b) resembles that of Fig. 1(c). This clearly indicates that the nonadiabatic-nondipole coupling is directly related to the effective angular frequency ω_{eff} . This motivates us to derive an analytical expression for $\langle p_z \rangle(\phi_p = 0)$ as a function of ω_{eff} , represented by dotted curves in Fig. 5. When the Coulomb potential is absent, $\phi_p = 0$ corresponds to $t = \pi/\omega$ within a single optical cycle. With these in mind, we find that the initial transverse momentum at $t = \pi/\omega$ is along the \hat{e}_x direction, with a magnitude given by [11]

$$v_\perp(t = \pi/\omega) = \frac{\sqrt{2I_p}}{6}\gamma_i + \frac{\sqrt{2I_p}}{6}\left(\frac{1}{9} - \frac{17\varepsilon^2}{60}\right)\gamma_i^3, \quad (29)$$

where the effective Keldysh parameter $\gamma_i = \frac{\omega_{\text{eff}}}{F}\sqrt{2I_p}$ with the instantaneous field strength $F(t = \pi/\omega) = \varepsilon F_0$ and the instantaneous effective angular frequency

$$\omega_{\text{eff}}\left(t = \frac{\pi}{\omega}\right) = \frac{\omega}{\varepsilon}. \quad (30)$$

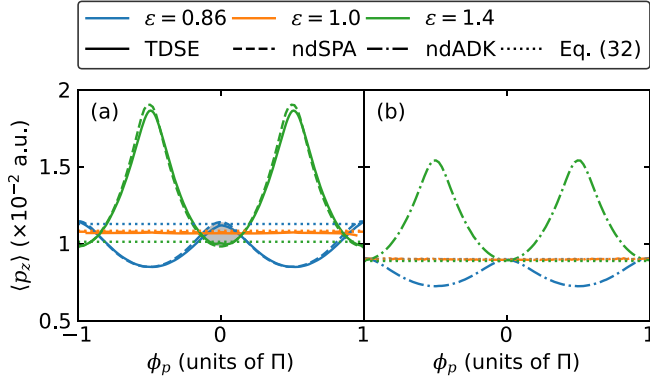


FIG. 5. Asymptotic linear momentum transfer $\langle p_z \rangle$ as a function of the photoemission angle ϕ_p for (a) nonadiabatic and (b) adiabatic tunneling calculated by TDSE (solid curves), ndSPA (dashed curves), and ndADK (dash-dotted curves). The average linear momentum transfer $\langle p_z \rangle$ around $\phi_p = 0$ can be expressed analytically by Eq. (32) (dotted curves). The shaded area in panel (a) is a clear indicator of nonadiabatic-nondipole coupling.

Thereby, we may obtain the linear momentum transfer at the tunnel exit

$$\langle v_{\perp} \rangle(\phi_p = 0) = a_1 \omega_{\text{eff}} + a_2 \omega_{\text{eff}}^3, \quad (31)$$

where a_1 and a_2 are given in Table I. It is further substituted for Eq. (6) to obtain the asymptotic linear momentum transfer

$$\begin{aligned} \langle p_z \rangle(\phi_p = 0) &= \langle p_z \rangle^{(A)}(\phi_p = 0) + \langle p_z \rangle^{(NA)}(\phi_p = 0) \\ &= (1 - \delta) \underbrace{\left(\frac{I_p}{3c} + \frac{\varepsilon F_0}{12c\sqrt{2I_p}} \right)}_A + \frac{A_0^2}{2c} \\ &\quad + \underbrace{b_1 \omega_{\text{eff}} + b_2 \omega_{\text{eff}}^2 + b_3 \omega_{\text{eff}}^3 + b_4 \omega_{\text{eff}}^4 + b_6 \omega_{\text{eff}}^6}_{\text{NA}}, \end{aligned} \quad (32)$$

where $\delta = (2\alpha_Z \varepsilon F_0)/(2I_p)^{3/2}$, $b_1 = \frac{A_0}{c} a_1$, $b_2 = \frac{1-\delta}{6c} a_1^2$, $b_3 = \frac{A_0}{c} a_2$, $b_4 = \frac{1-\delta}{3c} a_1 a_2$, and $b_6 = \frac{1-\delta}{6c} a_2^2$. Clearly, the linear momentum transfer has a positive correlation to the effective angular frequency ω_{eff} , up to order 6.

The dotted lines in Fig. 5(a) represent the sum of adiabatic and nonadiabatic contributions to the average linear momentum transfer $\langle p_z \rangle^{(A)}(\phi_p = 0) + \langle p_z \rangle^{(NA)}(\phi_p = 0)$ [Eq. (32)], corresponding to nonadiabatic tunneling, which agree very well with full TDSE and ndSPA calculations at $\phi_p = 0$. In Fig. 5(b), the dotted lines denote the adiabatic contribution $\langle p_z \rangle^{(A)}(\phi_p = 0)$ alone, where the intersection is clearly absent.

TABLE I. Analytical coefficients a_1 and a_2 for the average initial transverse momentum v_{\perp} in elliptically polarized (EP) laser fields and corotating (CoRTC) and counterrotating two-color (CRTC) circularly polarized laser fields around the photoemission angle $\phi_p = 0$ (EP fields) and $\phi_p = \pi$ (CoRTC and CRTC fields).

	EP ($\phi_p = 0$)	CoRTC ($\phi_p = \pi$)	CRTC ($\phi_p = \pi$)
a_1	$\frac{I_p}{3A_0\omega} - \frac{17}{90} \frac{I_p^2}{A_0^3\omega}$	$\frac{1}{3(1+\eta)} \frac{I_p}{A_0\omega}$	$\frac{1}{3(1-\eta)} \frac{I_p}{A_0\omega}$
a_2	$\frac{2}{27} \frac{I_p^2}{A_0^3\omega^3}$	$-\frac{31-210\eta-447\eta^2-248\eta^3}{270(1+2\eta)^3(1+\eta)^3} \frac{I_p^2}{A_0^3\omega^3}$	$-\frac{31+354\eta+465\eta^2-248\eta^3}{270(1+2\eta)^3(1-\eta)^3} \frac{I_p^2}{A_0^3\omega^3}$

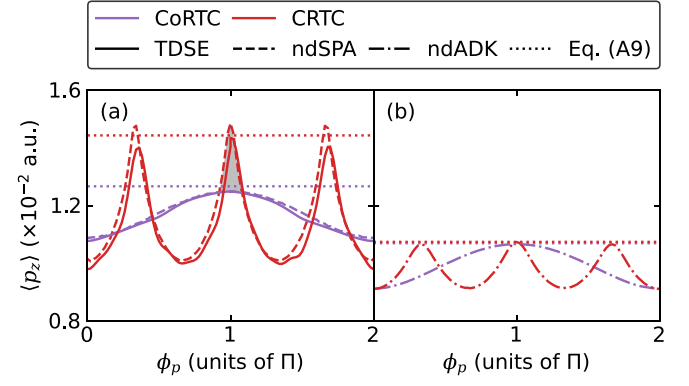


FIG. 6. Asymptotic linear momentum transfer $\langle p_z \rangle$ as a function of the photoemission angle ϕ_p for (a) nonadiabatic and (b) adiabatic tunneling calculated by TDSE (solid curves), ndSPA (dashed curves), and ndADK (dash-dotted curves). The average linear momentum transfer $\langle p_z \rangle$ around $\phi_p = \pi$ can be expressed analytically by Eq. (A9) (dotted curves). The shaded area in panel (a) is a clear indicator of nonadiabatic-nondipole coupling.

The analysis presented indicates that the intersection magnitude in the average linear momentum transfer can serve as a visual indicator of the nonadiabatic-nondipole coupling strength. To delve deeper into this relationship, we examine the correlation between the intersection magnitude in linear momentum transfer $\Delta\langle p_z \rangle$, which is the difference between the average linear momentum transfers for two distinct ellipticities, and the intersection magnitude in the effective angular frequency $\Delta\omega_{\text{eff}}$, both assessed at $\phi_p = 0$ in EP laser fields. Without loss of generality, we set one of the ellipticities as the reciprocal of the other, so that $\Delta\omega_{\text{eff}}$ can be expressed as

$$\Delta\omega_{\text{eff}}(\varepsilon) = \omega_{\text{eff}}(\varepsilon) - \omega_{\text{eff}}\left(\frac{1}{\varepsilon}\right), \quad (33)$$

and $\Delta\langle p_z \rangle$ is given by

$$\Delta\langle p_z \rangle(\varepsilon) = \langle p_z \rangle(\varepsilon) - \langle p_z \rangle\left(\frac{1}{\varepsilon}\right). \quad (34)$$

These variables are thereby studied as a function of ε , as shown in Figs. 9(a1) and 9(b1), respectively. As ε increases and gets closer to 1, ε gets closer to $1/\varepsilon$, and thus $\Delta\omega_{\text{eff}}$ decreases, as is clear from Fig. 9(a1), where the solid line is the numerical result and the dashed line represents the analytical value with $\omega_{\text{eff}}(\varepsilon)$ given by Eq. (30). Interestingly, the same trend shows up for $\Delta\langle p_z \rangle$, as illustrated in Fig. 9(b1), where the solid line denotes the numerical value obtained from ndSPA while the dashed line stands for the analytical

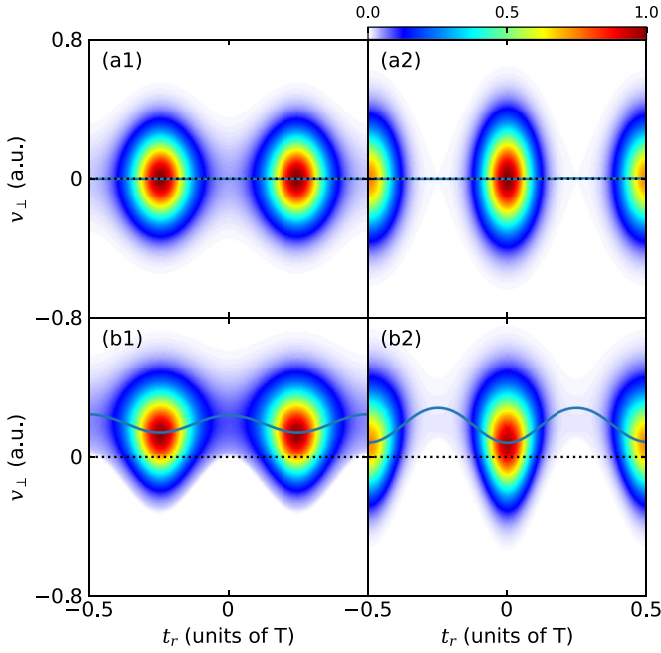


FIG. 7. The initial conditions prepared by the ndADK [row (a)] and ndSPA [row (b)] methods in the EP laser field with ellipticities $\varepsilon = 0.86$ [column (1)] and $\varepsilon = 1.4$ [column (2)]. The blue solid curves represent the average initial transverse momentum $\langle v_{\perp} \rangle$ as a function of ionization time t_r .

result with $\langle p_z \rangle(\varepsilon)$ given by Eq. (32). Clearly, the analytical result for the intersection magnitude in $\langle p_z \rangle$ largely reproduces the numerical one, both of which have a positive correlation with that in the effective angular frequency. Therefore, it can be concluded that $\Delta\omega_{\text{eff}}$ can be used to characterize the nonadiabatic-nondipole coupling strength.

Similar to the observations for EP fields, the intersection in the average linear momentum transfer at $\phi_p = \pi$, induced by the nonadiabatic-nondipole coupling effects, is also evident for CoRTC and CRTC fields in Fig. 6(a) when compared to the adiabatic tunneling scenario in Fig. 6(b), which can be traced back to the initial tunneling conditions of the electrons, as shown in Fig. 8. The derivation of the analytical expression for the linear momentum transfer at $\phi_p = \pi$ is provided in the Appendix, with results summarized in Table I. The magnitude of the intersection is on the level of 10^{-3} , within the detectable range of experimental measurements.

For CoRTC and CRTC fields, the positive correlation between the average linear momentum transfer and the effective angular frequency is also evident in Figs. 9(a2) and 9(b2). In this laser setup, the intersection magnitude in the average linear momentum is defined as the difference in $\langle p_z \rangle$ between CRTC and CoRTC fields, evaluated at $\phi_p = \pi$. The similar definition applies for the intersection magnitude in the effective angular frequency. Hence, $\Delta\omega_{\text{eff}}$ is given by

$$\Delta\omega_{\text{eff}}(\eta) = \omega_{\text{eff}}(\varepsilon = -1, \eta) - \omega_{\text{eff}}(\varepsilon = 1, \eta), \quad (35)$$

while $\Delta\langle p_z \rangle$ can be expressed as

$$\Delta\langle p_z \rangle(\eta) = \langle p_z \rangle(\varepsilon = -1, \eta) - \langle p_z \rangle(\varepsilon = 1, \eta). \quad (36)$$

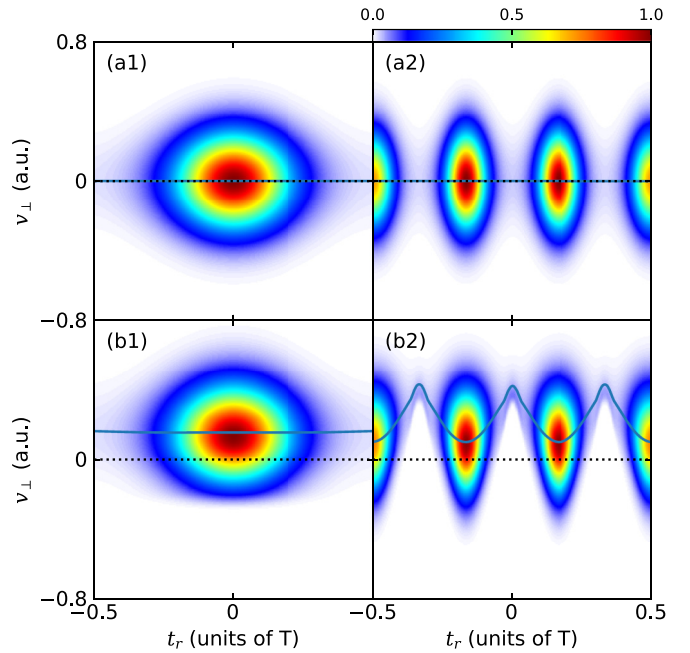


FIG. 8. The initial conditions prepared by the ndADK [row (a)] and ndSPA [row (b)] methods in the CoRTC field [column (1)] and the CRTC field [column (2)]. The blue solid curves represent the average initial transverse momentum $\langle v_{\perp} \rangle$ as a function of ionization time t_r .

These variables are thereby studied as a function of η , as shown in Figs. 9(a2) and 9(b2), respectively. As η increases, the ratio of the 2ω field over the ω field increases, leading to a higher effective angular frequency for the CRTC field and a lower effective angular frequency for the CoRTC field. Thereby, the difference between them enlarges, leading to the increasing trend of $\Delta\omega_{\text{eff}}$ as shown in Fig. 9(a2). Not surprisingly, the trend of $\Delta\langle p_z \rangle$ follows that of $\Delta\omega_{\text{eff}}$, as clear from Fig. 9(b2) for both numerical and analytical results, in the latter of which ω_{eff} and $\langle p_z \rangle$ are given by Eqs. (A1) and (A9), respectively. Therefore, intersection magnitude in the average linear momentum transfer can serve as a visual indicator of the nonadiabatic-nondipole coupling strength for CoCRTC and CRTC laser fields as well.

VI. CONCLUSIONS

In conclusion, we introduce two experimentally feasible protocols that facilitate the direct visualization of subcycle nonadiabatic-nondipole coupling effects, which have until now been elusive. We demonstrate the correlation between energy transfer and linear momentum transfer through the interplay of nonadiabatic and nondipole effects. By comparing the linear momentum transfer under nonadiabatic conditions, as calculated by ndSPA which includes coupling effects, with that under adiabatic conditions, as determined by ndADK where such effects are negligible, we can visually discern the impact of nonadiabatic-nondipole coupling on linear momentum transfer. This is evident in the form of a pronounced intersection in the average linear momentum transfer at a specific photoemission angle. The results from TDSE closely

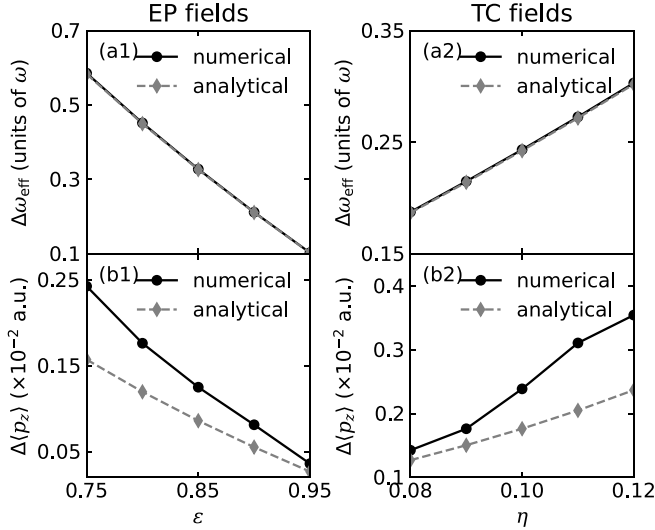


FIG. 9. Column (1): Intersection magnitude for the effective angular frequency $\Delta\omega_{\text{eff}}$ [panel (a1)] and the average linear momentum transfer $\Delta\langle p_z \rangle$ [panel (b1)] as a function of the ellipticity ε at $\phi_p = 0$ for the EP laser field. Column (2): Intersection magnitude for the effective angular frequency $\Delta\omega_{\text{eff}}$ [panel (a2)] and the average linear momentum transfer $\Delta\langle p_z \rangle$ [panel (b2)] as a function of the field ratio η at $\phi_p = \pi$ for the CoRTC and CRTC laser fields. The solid lines represent the numerical results, while dashed lines denote the analytical results of the intersection magnitude.

match those from ndSPA, validating the accuracy of the ndSPA method.

The detection of nonadiabatic-nondipole coupling effects is pivotally dependent on the choice of laser fields. First, the vector potential at a specific emission time should be consistent across multiple laser fields to ensure that the adiabatic term in Eq. (6) remains unchanged. Second, the effective angular frequencies of these laser fields should vary. With these conditions, the intersection in $\langle p_z \rangle$ emerges as the effective angular frequency varies, thereby highlighting the characteristics of the coupling effects. Remarkably, a more pronounced intersection indicates stronger coupling, while its absence suggests the absence of a coupling term. This phenomenon is observable in both EP laser fields with different ellipticities and in CoRTC and CRTC laser fields.

Additionally, we have derived the linear momentum transfer related to coupling effects as a function of the instantaneous effective angular frequency. Our work provides a means to observe subcycle nonadiabatic-nondipole coupling effects in linear momentum transfer, offering an intuitive understanding of the dynamics between energy and linear momentum transfer, thereby paving the pathway towards unraveling the complex interactions in strong-field ionization processes.

ACKNOWLEDGMENTS

This work was supported by the National Natural Science Foundation of China (Grants No. 92150105, No. 12474341, No. 12227807, and No. 12241407), the Science and Technology Commission of Shanghai Municipality (Grant No.

23JC1402000), and the Shanghai Pilot Program for Basic Research (Grant No. TQ20240204). Numerical computations were in part performed on the ECNU Multifunctional Platform for Innovation (001).

APPENDIX: LINEAR MOMENTUM TRANSFER AS A FUNCTION OF EFFECTIVE ANGULAR FREQUENCY IN CORTC AND CRTC LASER FIELDS

Similar to the case of EP laser fields, and the appearance of the average linear momentum transfer as shown in Fig. 6(a) for CoRTC and CRTC fields resembles that of the effective angular frequency presented in Fig. 2(c) as well, suggesting a direct connection between the nonadiabatic-nondipole coupling and the effective angular frequency. The effective angular frequency ω_{eff} at $t = 0$ is given by

$$\omega_{\text{eff}}(t = 0) = \left. \frac{\partial}{\partial t} \arctan \left(\frac{F_y}{F_x} \right) \right|_{t=0} = \omega \frac{1 + 2\eta}{1 + \varepsilon\eta}. \quad (\text{A1})$$

The nondipole tunneling effects have negligible impact on the PMD within the laser polarization plane [51]. Therefore, the initial transverse momentum $\mathbf{v}_\perp(\phi_p = \pi)$ can be derived within the dipole approximation. Accordingly, the ionization rate is given as, up to exponential accuracy,

$$W_{\text{SPA}}(\mathbf{p}) = \exp(-2\text{Im} S_D), \quad (\text{A2})$$

where $S_D = -\int_{t_s}^{t_r} \{[\mathbf{p} + \mathbf{A}(t)]^2/2 + I_p\} dt$. Taking the CoRTC field as an example,

$$S_D = \left\{ \left(\frac{p^2}{2} + I_p + U_p \right) t + \frac{A_0}{2\omega} \{ 2p_y [1 - \cos(\omega t)] + p_x \sin(\omega t) [2 + \eta \cos(\omega t)] + \eta p_y \sin^2(\omega t) \} + \frac{A_0^2}{6\omega} \eta \sin(3\omega t) \right\} \Big|_{t_r}^{t_s}, \quad (\text{A3})$$

where $U_p = [(1 + \eta^2/4)A_0^2]/2$, and thus

$$\text{Im} S_D = \left\{ \left(\frac{p^2}{2} + I_p + U_p \right) t_i + \frac{A_0}{2\omega} [2p_y \sin(\omega t_r) \sinh(\omega t_i) + 2p_x \cos(\omega t_r) \sinh(\omega t_i) + \frac{\eta}{2} p_x \cos(2\omega t_r) \sinh(2\omega t_i) + 2\eta p_y \cos(\omega t_r) \cosh(\omega t_i) \sin(\omega t_r) \sinh(\omega t_i) + \frac{A_0^2}{6\omega} \eta \cos(3\omega t_r) \sinh(3\omega t_i)] \right\}. \quad (\text{A4})$$

At $t_r = 0$, Eq. (A4) can be simplified as

$$\text{Im} S_D = \left\{ \left(\frac{p^2}{2} + I_p + U_p \right) t_i + \frac{A_0}{2\omega} p_x \left[2 \sinh(\omega t_i) + \frac{\eta}{2} \sinh(2\omega t_i) \right] + \frac{A_0^2}{6\omega} \eta \sinh(3\omega t_i) \right\}. \quad (\text{A5})$$

By requiring $\partial\{\text{Im} S_D\}/\partial \mathbf{p} = 0$, the most probable asymptotic momentum \mathbf{p} can be given as $p_y = p_z = 0$ and

$p_x = -(A_0/2)\{[2 \sinh(\omega t_i) + (\eta/2) \sin(2\omega t_i)]/(\omega t_i)\}$. Therefore, the corresponding initial transverse momentum is along the $-\hat{e}_x$ direction with a magnitude given by

$$\begin{aligned} v_{\perp}(t_r = 0) &= p_x + A_x \\ &= \frac{A_0}{2} \left[-\frac{2 \sinh(\omega t_i) + (\eta/2) \sin(2\omega t_i)}{\omega t_i} + (2+\eta) \right]. \end{aligned} \quad (\text{A6})$$

Obviously, the initial momentum \mathbf{v}_{\perp} and the vector potential \mathbf{A} are antiparallel at $t_r = 0$.

Subsequently, we establish the link between the initial transverse momentum and the effective angular frequency, ultimately deriving the linear momentum transfer as a function of the effective angular frequency. To this end, the tunneling time t_i can be expanded in powers of the instantaneous effective Keldysh parameter $\gamma_i = \omega_{\text{eff}} \sqrt{2I_p}/F(t_r)$,

$$\omega t_i = a\gamma_i + b\gamma_i^2 + d\gamma_i^3 + O(\gamma_i^4). \quad (\text{A7})$$

By solving the equation $\partial\{\text{Im}S_D\}/\partial t_i = 0$, we can obtain $a = (1 + \eta)/(1 + 2\eta)$, $b = 0$, and $c = [(-2 - 11\eta - 8\eta^2)/18](1 + \eta)/(1 + 2\eta)^3$. Substitution of them into Eq. (A6) yields the initial transverse momentum

$$\langle v_{\perp} \rangle(\phi_p = \pi) \approx v_{\perp}(t_r = 0) = a_1 \omega_{\text{eff}} + a_2 \omega_{\text{eff}}^3, \quad (\text{A8})$$

where the coefficients a_1 and a_2 are given in Table I. Likewise, we also derive the analytical coefficients for the CRTC field, which are also summarized in Table I.

Therefore, the asymptotic linear momentum transfer $\langle p_z \rangle$ at $\phi_p = \pi$ can be written as

$$\begin{aligned} \langle p_z \rangle(\phi_p = \pi) &= \langle p_z \rangle^{(\text{A})}(\phi_p = \pi) + \langle p_z \rangle^{(\text{NA})}(\phi_p = \pi) \\ &= (1 - \delta) \underbrace{\left(\frac{I_p}{3c} + \frac{F_0(1 + \varepsilon\eta)}{12c\sqrt{2I_p}} \right)}_{\text{A}} + \frac{A_0^2}{2c} \left(\frac{2 + \eta}{2} \right)^2 \\ &\quad + \underbrace{b_1 \omega_{\text{eff}} + b_2 \omega_{\text{eff}}^2 + b_3 \omega_{\text{eff}}^3 + b_4 \omega_{\text{eff}}^4 + b_6 \omega_{\text{eff}}^6}_{\text{NA}}, \end{aligned} \quad (\text{A9})$$

where $\delta = [2\alpha_Z F_0(1 + \varepsilon\eta)]/(2I_p)^{3/2}$. The expressions for b_1 through b_6 have the same form as those in the case of EP fields, i.e., $b_1 = \frac{2+\eta}{2} \frac{A_0}{c} a_1$, $b_2 = \frac{1-\delta}{6c} a_1^2$, $b_3 = \frac{2+\eta}{2} \frac{A_0}{c} a_2$, $b_4 = \frac{1-\delta}{3c} a_1 a_2$, and $b_6 = \frac{1-\delta}{6c} a_2^2$. Note that $\varepsilon = 1$ corresponds to the CoRTC field (purple dotted lines in Fig. 6) and $\varepsilon = -1$ corresponds to the CRTC field (red dotted lines in Fig. 6).

-
- [1] H. Reiss, Limits on tunneling theories of strong-field ionization, *Phys. Rev. Lett.* **101**, 043002 (2008).
- [2] H. Reiss, The tunnelling model of laser-induced ionization and its failure at low frequencies, *J. Phys. B* **47**, 204006 (2014).
- [3] M.-X. Wang, S.-G. Chen, H. Liang, and L.-Y. Peng, Review on non-dipole effects in ionization and harmonic generation of atoms and molecules, *Chin. Phys. B* **29**, 013302 (2020).
- [4] J. Maurer and U. Keller, Ionization in intense laser fields beyond the electric dipole approximation: Concepts, methods, achievements and future directions, *J. Phys. B* **54**, 094001 (2021).
- [5] M. Y. Ivanov, M. Spanner, and O. Smirnova, Anatomy of strong field ionization, *J. Mod. Opt.* **52**, 165 (2005).
- [6] S. V. Popruzhenko, Keldysh theory of strong field ionization: History, applications, difficulties and perspectives, *J. Phys. B* **47**, 204001 (2014).
- [7] Y. Ma, H. Ni, and J. Wu, Attosecond ionization time delays in strong-field physics, *Chin. Phys. B* **33**, 013201 (2024).
- [8] H. Ni, U. Saalman, and J.-M. Rost, Tunneling ionization time resolved by backpropagation, *Phys. Rev. Lett.* **117**, 023002 (2016).
- [9] H. Ni, U. Saalman, and J.-M. Rost, Tunneling exit characteristics from classical backpropagation of an ionized electron wave packet, *Phys. Rev. A* **97**, 013426 (2018).
- [10] M. Klaiber, K. Z. Hatsagortsyan, and C. H. Keitel, Under-the-tunneling-barrier recollisions in strong-field ionization, *Phys. Rev. Lett.* **120**, 013201 (2018).
- [11] K. Liu, S. Luo, M. Li, Y. Li, Y. Feng, B. Du, Y. Zhou, P. Lu, and I. Barth, Detecting and characterizing the nonadiabaticity of laser-induced quantum tunneling, *Phys. Rev. Lett.* **122**, 053202 (2019).
- [12] Z. Wang, W. Quan, X. Hao, J. Chen, and X. Liu, The ellipticity dependence of Rydberg state excitation of noble gas atoms subject to strong laser fields, *Front. Phys.* **11**, 1120654 (2023).
- [13] M. Klaiber, K. Z. Hatsagortsyan, and C. H. Keitel, Tunneling dynamics in multiphoton ionization and attoclock calibration, *Phys. Rev. Lett.* **114**, 083001 (2015).
- [14] S. Luo, M. Li, W. Xie, K. Liu, Y. Feng, B. Du, Y. Zhou, and P. Lu, Exit momentum and instantaneous ionization rate of nonadiabatic tunneling ionization in elliptically polarized laser fields, *Phys. Rev. A* **99**, 053422 (2019).
- [15] M. Li, J.-W. Geng, M. Han, M.-M. Liu, L.-Y. Peng, Q. Gong, and Y. Liu, Subcycle nonadiabatic strong-field tunneling ionization, *Phys. Rev. A* **93**, 013402 (2016).
- [16] D. Trabert, N. Anders, S. Brennecke, M. S. Schöffler, T. Jahnke, L. P. H. Schmidt, M. Kunitski, M. Lein, R. Dörner, and S. Eckart, Nonadiabatic strong field ionization of atomic hydrogen, *Phys. Rev. Lett.* **127**, 273201 (2021).
- [17] Z. Xiao, W. Quan, S. Yu, X. Lai, X. Liu, Z. Wei, and J. Chen, Nonadiabatic strong field ionization of noble gas atoms in elliptically polarized laser pulses, *Opt. Express* **30**, 14873 (2022).
- [18] I. Barth and O. Smirnova, Nonadiabatic tunneling in circularly polarized laser fields: Physical picture and calculations, *Phys. Rev. A* **84**, 063415 (2011).
- [19] I. Barth and O. Smirnova, Nonadiabatic tunneling in circularly polarized laser fields. II. Derivation of formulas, *Phys. Rev. A* **87**, 013433 (2013).
- [20] S. Eckart, K. Fehre, N. Eicke, A. Hartung, J. Rist, D. Trabert, N. Strenger, A. Pier, L. P. H. Schmidt, T. Jahnke, M. S. Schöffler, M. Lein, M. Kunitski, and R. Dörner, Direct experimental

- access to the nonadiabatic initial momentum offset upon tunnel ionization, *Phys. Rev. Lett.* **121**, 163202 (2018).
- [21] C. T. L. Smeenk, L. Arissian, B. Zhou, A. Mysyrowicz, D. M. Villeneuve, A. Staudte, and P. B. Corkum, Partitioning of the linear photon momentum in multiphoton ionization, *Phys. Rev. Lett.* **106**, 193002 (2011).
- [22] A. Ludwig, J. Maurer, B. W. Mayer, C. R. Phillips, L. Gallmann, and U. Keller, Breakdown of the dipole approximation in strong-field ionization, *Phys. Rev. Lett.* **113**, 243001 (2014).
- [23] B. Willenberg, J. Maurer, B. W. Mayer, and U. Keller, Sub-cycle time resolution of multi-photon momentum transfer in strong-field ionization, *Nat. Commun.* **10**, 5548 (2019).
- [24] A. Hartung, S. Eckart, S. Brennecke, J. Rist, D. Trabert, K. Fehre, M. Richter, H. Sann, S. Zeller, K. Henrichs *et al.*, Magnetic fields alter strong-field ionization, *Nat. Phys.* **15**, 1222 (2019).
- [25] M. Klaiber, E. Yakoboylu, H. Bauke, K. Z. Hatsagortsyan, and C. H. Keitel, Under-the-barrier dynamics in laser-induced relativistic tunneling, *Phys. Rev. Lett.* **110**, 153004 (2013).
- [26] S. Chelkowski, A. D. Bandrauk, and P. B. Corkum, Photon momentum sharing between an electron and an ion in photoionization: From one-photon (photoelectric effect) to multiphoton absorption, *Phys. Rev. Lett.* **113**, 263005 (2014).
- [27] S. Grundmann, M. Kircher, I. Vela-Perez, G. Nalin, D. Trabert, N. Anders, N. Melzer, J. Rist, A. Pier, N. Strenger *et al.*, Observation of photoion backward emission in photoionization of He and N₂, *Phys. Rev. Lett.* **124**, 233201 (2020).
- [28] M. Schmidt, N. Melzer, M. Kircher, G. Kastirke, A. Pier, L. Kaiser, P. Daum, D. Tsitsonis, M. Astaschov, J. Rist *et al.*, Role of the binding energy on nondipole effects in single-photon ionization, *Phys. Rev. Lett.* **132**, 233002 (2024).
- [29] S.-G. Chen, W.-C. Jiang, S. Grundmann, F. Trinter, M. S. Schöffler, T. Jahnke, R. Dörner, H. Liang, M.-X. Wang, L.-Y. Peng, and Q. Gong, Photon momentum transfer in single-photon double ionization of helium, *Phys. Rev. Lett.* **124**, 043201 (2020).
- [30] F. Sun, X. Chen, W. Zhang, J. Qiang, H. Li, P. Lu, X. Gong, Q. Ji, K. Lin, H. Li *et al.*, Longitudinal photon-momentum transfer in strong-field double ionization of argon atoms, *Phys. Rev. A* **101**, 021402(R) (2020).
- [31] P.-L. He, D. Lao, and F. He, Strong field theories beyond dipole approximations in nonrelativistic regimes, *Phys. Rev. Lett.* **118**, 163203 (2017).
- [32] H. Liang, M.-X. Wang, X.-R. Xiao, Q. Gong, and L.-Y. Peng, Photon-momentum transfer in diatomic molecules: An *ab initio* study, *Phys. Rev. A* **98**, 063413 (2018).
- [33] A. Hartung, S. Brennecke, K. Lin, D. Trabert, K. Fehre, J. Rist, M. S. Schöffler, T. Jahnke, L. P. H. Schmidt, M. Kunitski *et al.*, Electric nondipole effect in strong-field ionization, *Phys. Rev. Lett.* **126**, 053202 (2021).
- [34] X. Mao, H. Ni, X. Gong, J. Burgdörfer, and J. Wu, Subcycle-resolved strong-field tunneling ionization: Identification of magnetic dipole and electric quadrupole effects, *Phys. Rev. A* **106**, 063105 (2022).
- [35] M. M. Lund and L. B. Madsen, Nondipole photoelectron momentum shifts in strong-field ionization with mid-infrared laser pulses of long duration, *J. Phys. B* **54**, 165602 (2021).
- [36] S. Brennecke and M. Lein, Nondipole modification of the ac Stark effect in above-threshold ionization, *Phys. Rev. A* **104**, L021104 (2021).
- [37] K. Lin, S. Eckart, A. Hartung, D. Trabert, K. Fehre, J. Rist, L. P. H. Schmidt, M. S. Schöffler, T. Jahnke, M. Kunitski, and R. Dörner, Photoelectron energy peaks shift against the radiation pressure in strong-field ionization, *Sci. Adv.* **8**, eabn7386 (2022).
- [38] H. Ni, S. Brennecke, X. Gao, P.-L. He, S. Donsa, I. Březinová, F. He, J. Wu, M. Lein, X.-M. Tong, and J. Burgdörfer, Theory of subcycle linear momentum transfer in strong-field tunneling ionization, *Phys. Rev. Lett.* **125**, 073202 (2020).
- [39] V. P. Majety and A. Scrinzi, Absence of electron correlation effects in the helium attoclock setting, *J. Mod. Opt.* **64**, 1026 (2017).
- [40] S. Brennecke and M. Lein, High-order above-threshold ionization beyond the electric dipole approximation, *J. Phys. B* **51**, 094005 (2018).
- [41] N. J. Kylstra, R. Potvliege, and C. Joachain, Photon emission by ions interacting with short intense laser pulses: Beyond the dipole approximation, *J. Phys. B* **34**, L55 (2001).
- [42] G. F. Gribakin and M. Y. Kuchiev, Multiphoton detachment of electrons from negative ions, *Phys. Rev. A* **55**, 3760 (1997).
- [43] T. K. Kjeldsen and L. B. Madsen, Strong-field ionization of atoms and molecules: The two-term saddle-point method, *Phys. Rev. A* **74**, 023407 (2006).
- [44] D. Milošević, G. Paulus, D. Bauer, and W. Becker, Above-threshold ionization by few-cycle pulses, *J. Phys. B* **39**, R203 (2006).
- [45] N. Eicke and M. Lein, Attoclock with counter-rotating bicircular laser fields, *Phys. Rev. A* **99**, 031402(R) (2019).
- [46] N. Eicke, S. Brennecke, and M. Lein, Attosecond-scale streaking methods for strong-field ionization by tailored fields, *Phys. Rev. Lett.* **124**, 043202 (2020).
- [47] S. Eckart, M. Richter, M. Kunitski, A. Hartung, J. Rist, K. Henrichs, N. Schlott, H. Kang, T. Bauer, H. Sann *et al.*, Nonsequential double ionization by counterrotating circularly polarized two-color laser fields, *Phys. Rev. Lett.* **117**, 133202 (2016).
- [48] M. Han, P. Ge, Y. Shao, Q. Gong, and Y. Liu, Attoclock photoelectron interferometry with two-color corotating circular fields to probe the phase and the amplitude of emitting wave packets, *Phys. Rev. Lett.* **120**, 073202 (2018).
- [49] P. Ge, M. Han, Y. Deng, Q. Gong, and Y. Liu, Universal description of the attoclock with two-color corotating circular fields, *Phys. Rev. Lett.* **122**, 013201 (2019).
- [50] P. Ge, Y. Fang, Z. Guo, X. Ma, X. Yu, M. Han, C. Wu, Q. Gong, and Y. Liu, Probing the spin-orbit time delay of multiphoton ionization of Kr by bicircular fields, *Phys. Rev. Lett.* **126**, 223001 (2021).
- [51] Y. Ma, J. Zhou, P. Lu, H. Ni, and J. Wu, Influence of nonadiabatic, nondipole and quantum effects on the attoclock signal, *J. Phys. B* **54**, 144001 (2021).